Materials Advances

ROYAL SOCIETY OF CHEMISTRY

PAPER

View Article Online
View Journal | View Issue

Cite this: *Mater. Adv.*, 2023, 4, 5817

Chiral mesostructured hydroxyapatite on 3D macroporous coralline scaffolds for enantio-selective osteogenesis†

Chao Zhou,‡[a] Anqi Liu,‡[bc] Ping Li,‡[d] Jing Ai,[e] Lu Han,[e] Shaoyang Zhang,[d] Shuai Chen,[a] Yuanming Ouyang,*[a] Baojie Li,*[d] Shunai Che*[f] and Cunyi Fan*[a]

Chirality is ubiquitous in nature from the macroscopic to microscopic scale, and plays an important role in life. Natural bone combines stiffness and toughness, and is formed by assembling collagen and minerals with a chiral mesostructure from the atomic to macroscopic scales. Bone inspired bio-scaffolds have been extensively investigated to construct the microenvironment closest to bone structure, including roughened surface, three dimensional structure and hierarchical structure. However, the chiral hierarchical structure is not reflected in the current bone repair materials. Here, we designed a bone repair scaffold chiral mesostructured hydroxyapatite on corallite (CMHAP@CL) for osteogenesis promotion *in vivo*, which integrates a three-dimensional porous structure, hierarchical structure and chiral mesostructure. The CMHAP films with thicknesses of ~13.6 μm were grown on 3D microporous (aperture 100–300 μm) CL substrates with chiral hierarchical structures ranging from the atomic to macro scale. We found that the L-CMHAP@CL scaffolds synthesized with L-tartaric acid accelerated angiogenesis and osteogenesis, whereas the D-CMHAP@CL and Ach-MHAP@CL scaffolds synthesized with D-tartaric acid and free chiral molecule had a weaker effect. This chiral selectivity was speculated to be derived mainly from the bioadaptivity between the space configuration of the osteoblast and the chiral hierarchical structure. These findings will facilitate the development of the design of biomaterials for bone regeneration and clinical application.

Received 28th September 2023,
Accepted 21st October 2023

DOI: 10.1039/d3ma00773a

rsc.li/materials-advances

1. Introduction

Chirality, one of the most important codes in organisms, has a regulatory effect on various biological activities, because the enantiomer selectivity of chiral substances in biological systems is vital for maintaining normal organism functions.[1,2] In bone, the extracellular matrix is primarily composed of type-I collagen (a chiral biomacromolecule) as the organic matrix phase and ion-substituted, carbonated apatite as the inorganic reinforcing phase.[3,4] Chiral collagen serves as a structural template that, in conjunction with mineralization inhibitors, regulates the process of mineralization, directs subsequent crystal growth, and governs the size and distribution of apatite crystals within bone.[5,6] Previous studies have reported that bone minerals have hierarchical structures from nano to macroscopic scales.[7–9] Furthermore, in our recent work, it has been demonstrated that the inorganic component in bone presents a hierarchical chiral arrangement, from the twisted mineral crystals surrounding a collagen fibril to spiral fibers to helix bundles to whole bone.[10]

Bone defects caused by bone tumors, trauma, infection and deformity are common clinical problems, for which limb

[a] *Department of Orthopaedics, Shanghai Engineering Research Center for Orthopaedic Material Innovation and Tissue Regeneration, Shanghai Sixth People's Hospital Affiliated to Shanghai Jiao Tong University School of Medicine, 600 Yishan Road, Shanghai 200233, China. E-mail: ouyangyuanming@163.com, cyfan@sjtu.edu.cn*

[b] *Department of Orthodontics, Shanghai Stomatological Hospital & School of Stomatology, Fudan University, Beijing East Road No. 356, Shanghai 200001, China*

[c] *Huangpu District, Shanghai Key Laboratory of Craniomaxillofacial Development and Diseases, Fudan University, Tianjin Road No. 2, Huangpu District, Shanghai, 200001, China*

[d] *Bio-X Center, Key Laboratory for the Genetics of Developmental and Neuropsychiatric Disorders, Ministry of Education, Shanghai Jiao Tong University, 800 Dongchuan Road, Shanghai, 200240, China. E-mail: libj@sjtu.edu.cn*

[e] *School of Chemical Science and Engineering, Tongji University, 1239 Siping Road, Shanghai, 200092, China*

[f] *School of Chemistry and Chemical Engineering, State Key Laboratory of Composite Materials, Frontiers Science Center for Transformative Molecules, Shanghai Key Laboratory for Molecular Engineering of Chiral Drugs, Shanghai Jiao Tong University, 800 Dongchuan Road, Shanghai, 200240, China. E-mail: chesa@sjtu.edu.cn*

† Electronic supplementary information (ESI) available. See DOI: https://doi.org/10.1039/d3ma00773a

‡ These authors contributed equally to this work.

treatment can be difficult, resulting in complicated surgery with a long timescale, many complications, and high disability rate and amputation rate. They often result in serious burdens on individuals, families and the social economy, and frequently call for surgical intervention.[11,12] The main surgical treatment methods for bone defects are fibula autograft, bone transport, induced membrane treatment, *etc.* These techniques have achieved certain clinical therapeutic effects, but there are also some shortcomings that cannot be ignored.[13,14] Therefore, bone repair materials have become an effective way to treat bone defects.[15–17] At present, bone repair materials include osteogenic active materials, metal prostheses, 3D printed prostheses, *etc.* All of these materials present limitations in achieving the requirements for bone repair materials, especially structure matching and osteoinductive capabilities.[18]

To improve the matching capacity and osteoinductive potential of bone scaffold materials, the use of bionic structure design has been widely explored. Nanostructures have been proved to promote osteogenesis, therefore, researchers have used electron beam direct writing technology to prepare hierarchical structures ranging from 10 nm to a micron to induce osteogenesis, and its effectiveness has been demonstrated.[19] Natural bone has a complex three-dimensional porous structure. 3D printing technology can biochemically mimic three-dimensional ordered structures, and can effectively simulate the three-dimensional microenvironment in bone.[20] In addition, similar structures of lamellar bone and cancellous bone can be imitated by adjusting and optimizing structural parameters, controlling pore size, pore shape and connectivity.[21] Studies have also shown that a surface with certain physical and chemical properties can be prepared by a high temperature annealing process, which can enhance cell adhesion and promote osteogenic differentiation of osteoblasts, and effectively improve bone growth and bone integration.[22] The surface coating modification technology is also effective in improving the biological activity of osteogenic materials. Research shows that porous piezoelectric ceramics coated on a titanium alloy surface can improve the surface roughness and biocompatibility of the material. Cell experiments demonstrated that $BaTiO_3$ piezoelectric ceramics can enhance the osteogenic differentiation of BMMSCs, thereby promoting bone growth and integration.[23] In addition, a topological surface structure has also been shown to mediate immune regulation to improve bone repair performance, and further regulate the bone growth process by influencing the adhesion and interaction of progenitor cells and immune cells through topological morphology.[24] However, all of these designed materials lack the most important factor of a chiral microenvironment, which plays a significant role in natural bone structure. Therefore, how to construct a bioadaptive bone repair material that closely simulates the microenvironment of the natural bone tissue structure is a key scientific problem to be solved urgently for the repair of bone defects.[25,26] In this paper, our goal was to design a bone-repair biomaterial combining a 3D configuration, hierarchical structure and chiral microenvironment, which selectively promotes osteogenesis *in vivo*.

2. Synthesis of CMHAP@CL

We *in situ* grew chiral hierarchical structured hydroxyapatite (HAP) nanoplates on a corallite (CL) substrate by means of a facile chiral tartaric acid (TTA) molecule induced self-assembly strategy (Fig. S1, ESI†). The substrate was not treated additionally other than being washed with water and ethyl alcohol. The chiral mesostructured hydroxyapatite (CMHAP) nanoplates were *in situ* grown on the CL substrate from a homogeneous solution composed of tartaric acid, urea, ammonium dihydrogen phosphate, and deionized water under hydrothermal conditions. The first step is the hydrothermal decomposition of the CL substrate to form Ca^{2+}. Then, D/L-TTA was chosen as both a structure-directing and symmetry-breaking agent for the asymmetric attachment and co-self-assembly process with Ca^{2+} ions due to its complexation behavior. The urea decomposed slowly and controlled the process of crystal growth. Ca^{2+} ions in solution would precipitate slowly because urea breaks down and forms an alkaline environment, thus facilitating the formation of chiral HAP nanosheets.[27] The CMHAP@CL scaffolds were collected by taking out the CL substrate from the synthesis solution. The scaffolds synthesized with L-TTA and D-TTA were defined as L-CMHAP@CL and D-CMHAP@CL, respectively. For a comparison, achiral MHAP was deposited on the CL with a free chiral molecule, which was denoted as Ach-MHAP@CL. The scaffolds were then used as osteogenic materials *in vivo* in our subsequent research.

3. Results and discussion

3.1 Structural characterizations of CMHAP@CL

The antipodal CMHAP@CL scaffolds are grayish-white in colour with a porous and topological surface (Fig. 1(a_1) and Fig. S2, ESI†). Fig. 1(a_1)–(a_4) shows scanning electron microscopy (SEM) images with different magnifications of the L-CMHAP@CL scaffolds. The CMHAP film is composed of densely packed nanoplates, with widths ranging from 200 to 500 nm, thicknesses between 20 and 50 nm, and heights reaching up to 13.6 μm. These nanoplates grow vertically from the surface of the CL substrate (Fig. S3, ESI†). Left-handed helical stacking of nanoplates (as shown in Fig. 1(a_3)) is considered as the tertiary level of chirality, indicating a high degree of structural complexity and potential for advanced applications. The magnified SEM image (Fig. 1(a_4)) reveals that the nanoplates are fragmented into multiple nanoflakes with widths ranging from 20 to 150 nm. Additionally, the left-handed helical arrangement of nanoflakes can be observed within the nanoplates, which is considered as a secondary level chirality of the CMHAP@CL scaffolds.

High-resolution transmission electron microscopy (HRTEM) investigations confirmed the secondary and primary chirality, as well as the fine crystalline structure of the nanoflakes. Fig. 1(b) shows the HRTEM image and corresponding Fourier diffractograms (FDs) of a single nanoplate and three adjacent nanoflakes. The nanoplate comprises three adjacent nanoflakes arranged side by side. The FDs were generated in three

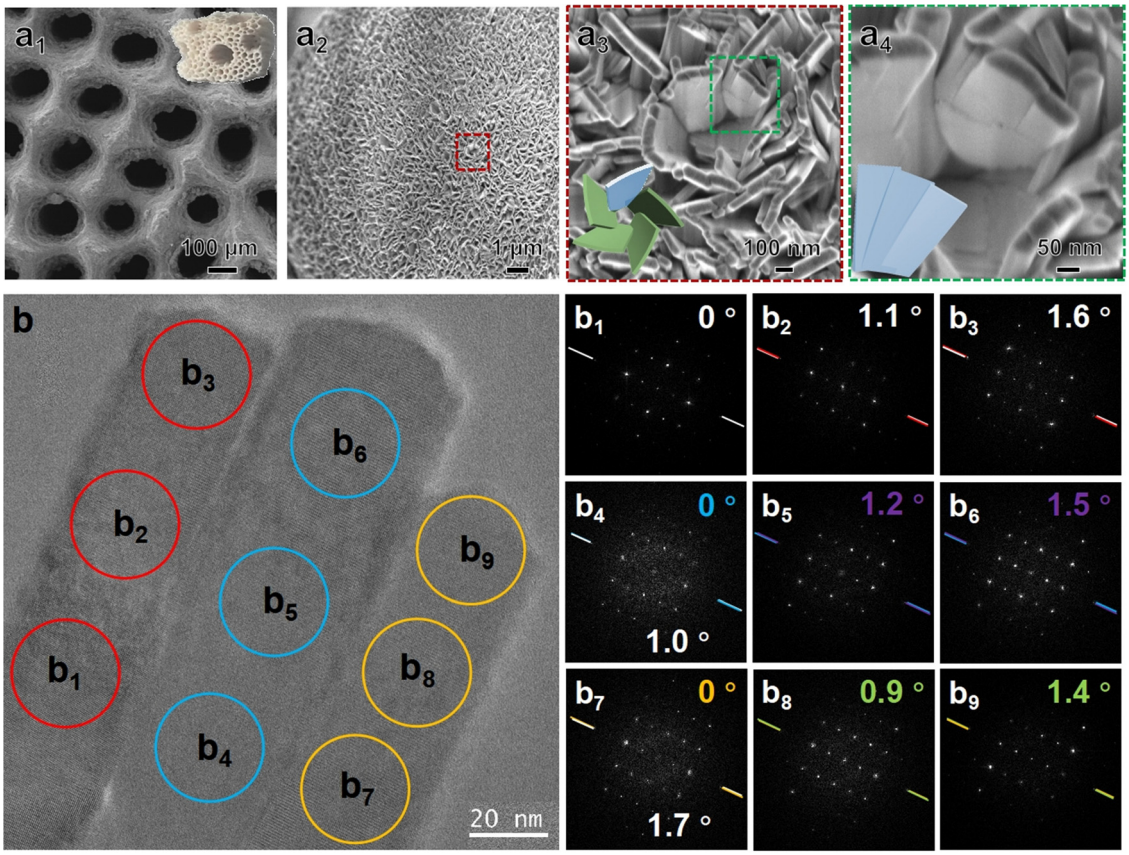

Fig. 1 Morphology and chiral structure of L-CMHAP@CL. (a_1)–(a_4) Photograph and SEM images of L-CMHAP@CL at varying magnifications. (b) TEM image and corresponding FD patterns of the nanoplate taken from the [1−100] axis. The synthetic molar composition was 1 L-TTA: 2 corallite: 1 $NH_4H_2PO_4$: 2.23 CON_2H_4: 1667 H_2O.

local areas of each nanoflake to determine crystal orientation and arrangement. The nanoflakes can be identified as being oriented along the [1−100] direction of the HAP structure based on analysis of the HRTEM image and FD data. The crystal is oriented along the [−1−120] axis with its long edge perpendicular to the substrate during growth. A slight angular deviation of approximately 1.7° can be discerned between the FDs obtained from adjacent nanoflakes at comparable elevations (Fig. 1(b_1), (b_4) and (b_7)), indicating a minute displacement between the nanoflakes with a small angle. This is in line with the SEM observation of secondary-level chirality. Additionally, the FDs of three consecutive positions along each nanoflake's axial direction exhibit identical crystal orientation with a continuous rotation at an infinitesimal angle. The intensity variation of diffraction spots also indicates misalignment of crystal orientation to the electron beam due to continuous twisting of the crystal lattice, which is considered as CMHAP@CL's primary chirality. Although determining the handedness of primary chirality can be challenging due to the potential for antipodal chiral structures to experience similar orientation relationships in FDs, a fractal-like left-handed twist may be inferred based on the rotational direction of the twisted nanoplate.[28,29] D-CMHAP@CL scaffolds possess an identical structure but with a reversed arrangement (Fig. S2, S4 and S5, ESI†).

The crystalline structure of L-CMHAP@CL scaffolds was further analyzed by means of wide-angle X-ray diffractometry (XRD) to obtain more detailed information. The XRD patterns of the L-CMHAP@CL scaffolds and CL are depicted in Fig. 2(a). Although the CL substrate exhibited a stronger intensity in the XRD pattern of CMHAP@CL, the characteristic reflections of HAP's hexagonal phase with space group P63/*m* and lattice parameters of $a = b = 9.4166$ Å and $c = 6.8745$ Å [JCPDS file 09-0432] can still be identified (see the purple asterisk position in Fig. 2(a) and (b)).

Therefore, we have proposed a structural model and a plausible transfer mechanism to elucidate the hierarchical chirality of CMHAP@CL scaffolds, using L-CMHAP@CL as an example. (See ESI,† Fig. S6 and detailed description.)

The chirality of the CMHAP@CL scaffolds was unambiguously determined through optical activity (OA) analysis using diffuse reflectance ultraviolet-visible (DRUV-Vis) and circular dichroism (DRCD) spectroscopy, due to the opaqueness of the scaffolds (Fig. 2(c)). DRCD with white and black backgrounds exhibit predominantly absorption-based OA (AOA) and both scattering-based OA (SOA) and AOA, respectively, due to the reflection of almost all visible light by the white background and absorption by the black backboard (Fig. S7, ESI†). The semiconductor nanounits aggregate in a chiral manner, with distances shorter than the Bohr exciton radius. This induces a

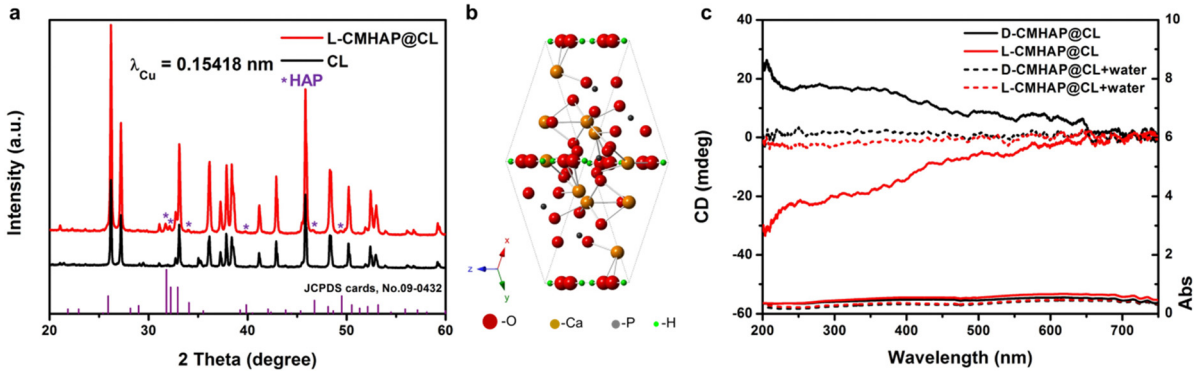

Fig. 2 Crystal structure and multiple OAs of the CMHAP@CL. (a) XRD patterns of L-CMHAP@CL (red line) and the CL substrate. Reflections of CL are labelled with a black line, λ_{Cu} = 1.5418 Å, HAP JCPDS cards. No. 09-0432. (b) a single crystal cell structure of the HAP nanoplates. (c) DRUV-Vis and DRCD spectra of the antipodal CMHAP@CL shown in Fig. 1(a) (red line, L-CMHAP@CL) and Fig. S2 (ESI†) (black line, D-CMHAP@CL) measured with a black background.

dissymmetric field on the entire aggregate through excitation delocalization, resulting in AOA based on electronic transition.[30,31] The SOA is observed at multiple integral wavelengths determined by $m\lambda = Pn_{avg}$, where m is an integer, n_{avg} is the average refractive index and P is the pitch length of the chiral medium.[32–34] A chiral structure with left-handedness exhibits a preference for absorbing right-handed circularly polarized light and reflecting left-handed light, leading to negative angles of arrival and sum of angle signals in the measurement of differential reflection circular dichroism. As shown in Fig. 2(c), the L-CMHAP@CL and D-CMHAP@CL scaffolds showed mirror-imaged signals at 200–700 nm. Using L-CMHAP@CL as an example, the UV-Vis spectrum exhibited three broad bands spanning 200–250 nm, 250–480 nm, and 480–700 nm. Meanwhile, the CD spectrum displayed two negative shoulders and intense peaks at approximately 208 nm, as well as in the ranges of 250–480 nm and 480–650 nm. According to the detection mechanism, the OA of CMHAP@CL scaffolds comprises both AOA and SOA due to the CL substrate being seen as a black background. After infiltration with water, the absorbance band within the range of 200–700 nm exhibited a slight decrease, while that within the range of 200–480 nm remained (see the red dotted line in Fig. 2(c) showing the absorbance). As a result, the CD spectra exhibit a weak negative broad peak centered at approximately 303 nm, which corresponds to characteristic electron transitions of HAP with band gaps measuring 3.9 eV.[35,36] Furthermore, the scattering-based OA experienced a significant reduction (indicated by the red dotted line in Fig. 2(c)) due to the disappearance of an optical chiral interface caused by decreasing differences in refractive indices between HAP and air *versus* HAP and water. Thus, the CMHAP@CL scaffolds exhibited both AOA and SOA at approximately 303 nm and approximately 208 and 350 nm, respectively. The mirror-imaged DRCD spectrum of D-CMHAP@CL scaffolds indicated the opposite handedness.

The DRCD spectra of CL (Fig. S8, ESI†) and TTA (Fig. S9, ESI†) confirmed that the OAs of the CMHAP@CL scaffolds were attributed to the hierarchical chiral structures, rather than chiral imprinting from chiral molecules or CL substrates. Ach-MHAP@CL exhibits a morphology similar to that of antipodal CMHAP@CL scaffolds but without chirality (Fig. S2 S4, S5 and S10, ESI†).

3.2 Osteogenic activity of CMHAP@CL

A multitude of studies demonstrate that marine coral derived from the exoskeleton of madreporic corals is a promising biomaterial, exhibiting porosity comparable to human cancellous or cortical bone and possessing bioresorbable, adequate mechanical, and inherent osteoconductive properties.[37] Converted coralline hydroxyapatite has been utilized in bone grafts and orbital implants due to its exceptional pore interconnectivity, which allows for the infiltration of blood vessels, and its excellent biocompatibility with no cytotoxicity.[38] Our previous work demonstrated that chiral mesostructured hydroxyapatite has a selective regulatory effect on osteogenic differentiation of bone marrow mesenchymal stem cells.[39] Therefore, in this paper, the *in vivo* osteogenic activity of CMHAP@CL was studied in detail.

The experiment was performed on nude mice, each carrying duplicates of three sample types: Ach-MHAP@CL, L-CMHAP@CL and D-CMHAP@CL (Fig. 3(a)). Control scaffolds, called Ach-MHAP@CL, were synthesized with free chiral molecules. The animals were euthanized at 12 and 24 weeks post-implantation, and the grafts were subsequently extracted and processed for histological analysis.

In order to quantify the bone formation ability of the chiral scaffolds, Scanco μ-CT50 was used to characterize the scaffolds 12 weeks after osteogenesis *in vivo* from a three-dimensional perspective. Fig. 3(b) shows the CT scan results of the material tissue after osteogenesis. *X*/*Y*, *X*/*Z* and *Z*/*Y* are two-dimensional views of different sections of the post-osteogenic scaffold material tissue. It could be clearly seen that new bone tissue was formed both inside and outside the pores of the scaffold. The images showed the ROI (study image area) of all the extracted pores. Different components were analyzed *via* different thresholds. The yellow part represents the hydroxyapatite

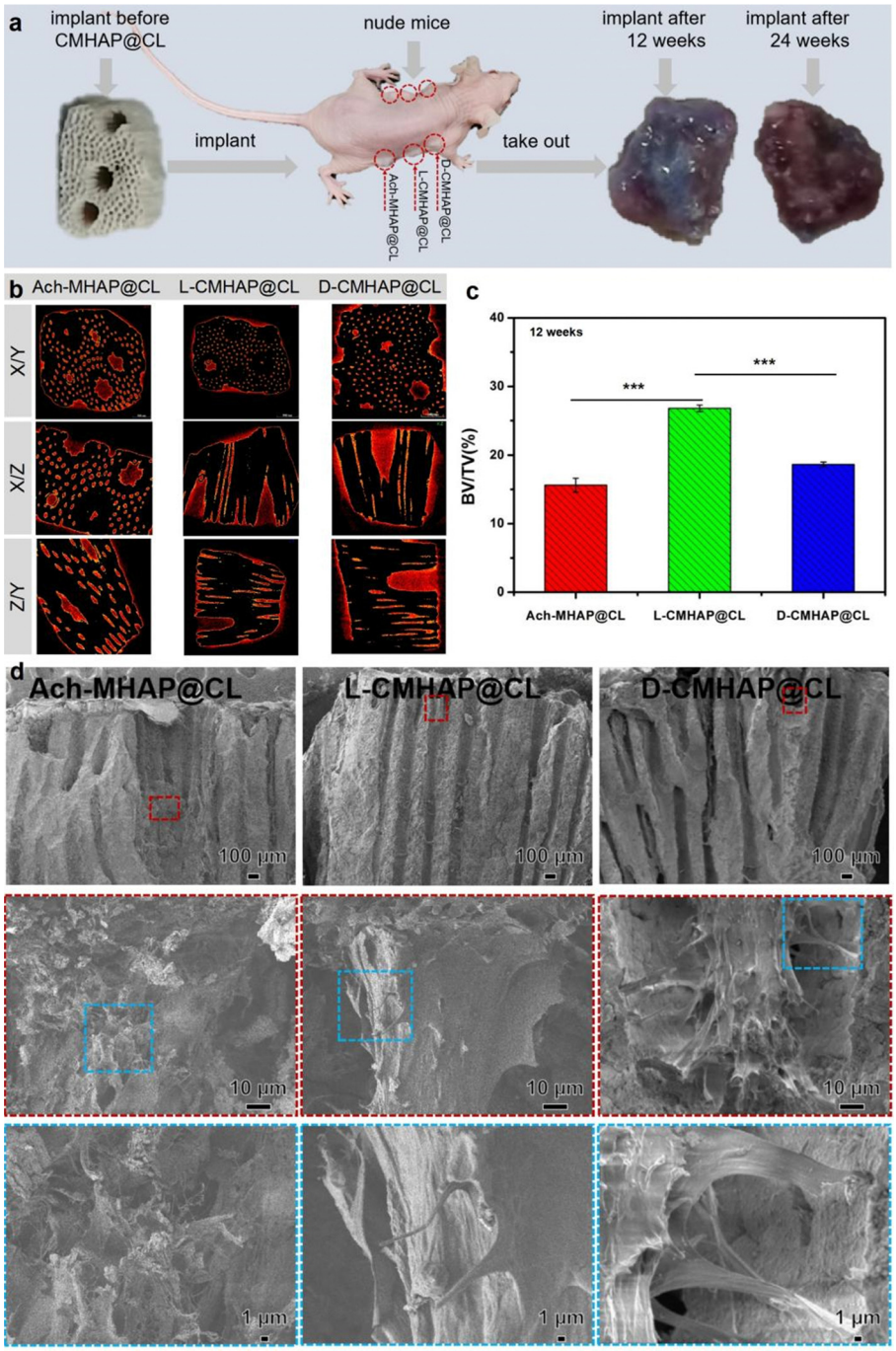

Fig. 3 Selective promoted bone formation of CMHAP@CL after 12 weeks of implantation subcutaneously on both sides of the abdomen in nude mice. (a) Photographs of implantation of the CMHAP@CL scaffolds on both sides of the abdominal cavity of nude mice and before and after implantation with CMHAP@CL. There were three mice used in the surgical experiment as a parallel group, each carrying a duplicate of the three scaffold types: L-CMHAP@CL, D-CMHAP@CL and Ach-MHAP@CL (the control). Photo images show the scaffolds implanted subcutaneously in nude mice and a harvested highly vascularized and ossification implant after 12 and 24 weeks. (b) After implantation for 12 weeks, the samples were detected using micro-CT. The typical inner 2D sectional images were captured to display the newly formed bone in the pores (regions within the yellow circles). (c) Bone volume fraction at 12 weeks post-surgery (n = 6). (d) SEM images showing the osteogenic assessment of collagen fibrils. Notice the rougher and more mature collagen fibres in L-CMHAP@CL in comparison with D-CMHAP@CL and Ach-MHAP@CL. Data are presented as mean ± SD. *$P < 0.05$, **$P < 0.01$, ***$P < 0.001$.

scaffold layer while the red part indicates newly formed bone. 12 weeks after implantation, the L-CMHAP@CL scaffolds presented superior new bone tissue compared to the D-CMHAP@CL scaffolds and Ach-MHAP@CL scaffolds. X/Z and Y/Z views of the two-dimensional section images revealed that the L-CMHAP@CL scaffolds showed more intraperitoneal

osteogenesis and a larger percentage of pore filling compared to the D-CMHAP@CL scaffolds and Ach-MHAP@CL scaffolds.

In addition, morphometrical analysis (Fig. 3(c)) showed that the bone volume/tissue volume (BV/TV) value of the L-CMHAP@CL scaffolds (26.8% ± 0.47%) was significantly higher than that of the other two groups, the D-CMHAP@CL scaffolds (18.7% ± 0.35%) and Ach-MHAP@CL scaffolds (15.6% ± 1.02%). As shown in Fig. S11 and S12 (ESI†), the CT scan results for 24 weeks after implantation also showed a similar trend. These results indicated that, compared with the D-CMHAP@CL and Ach-MHAP@CL scaffolds, the L-CMHAP@CL scaffolds promoted bone growth more significantly.

From the perspective of material science, the scaffolds were characterized by scanning electron microscopy (SEM) after 12 weeks of implantation *in vivo*. The sample treatment methods were as follows: first, the scaffold material after osteogenesis was removed from the mouse, and then fixed in paraformaldehyde solution. Second, the scaffold material was dehydrated by ethanol with a gradient concentration several times, and then dried by vacuum drying at room temperature. Finally, the sample was fixed on a sample table for SEM observation. The results are shown in Fig. S13 (ESI†), indicating low and high morphologies of blank scaffolds without bone growth, Ach-MHAP@CL scaffolds, L-CMHAP@CL scaffolds and D-CMHAP@CL scaffolds at 12 weeks of *in vivo* osteogenesis. It could be seen that the blank scaffold material was in a three-dimensional porous structure, and its surface was covered with a thin film formed by an ordered sheet hydroxyapatite assembly. The pores in the scaffold were filled with new bone and the scaffold's whole surface was covered with bone tissue after 12 weeks of osteogenesis *in vivo*. Enlarged SEM images showed that the collagen fibers formed on the L-CMHAP@CL scaffolds were dense and orderly, and the typical periodic structure of mineralized collagen fibers was clearly observed. However, the classical periodic arrangements of mineralized collagen fibers formed on the D-CMHAP@CL scaffolds and Ach-MHAP@CL scaffolds are relatively sparse and less well-ordered than those on the L-CMHAP@CL scaffolds.

As shown in Fig. 3(d), SEM observation of the cross-section morphology of the scaffolds after 12 weeks of *in vivo* osteogenesis clearly showed that the pore interior of the blank scaffold material was smooth, and the pore diameter of the scaffold material after *in vivo* osteogenesis was small. The surface of the pore wall was rough, and the new bone tissue growing inside the pore could be clearly seen. Furthermore, there was also bone formation deep inside the tunnels. A comparison of the Ach-MHAP@CL scaffolds, L-CMHAP@CL scaffolds and D-CMHAP@CL scaffolds revealed that the L-CMHAP@CL scaffolds led to a more pronounced increase in bone formation, which is consistent with the previous surface observations. The above results indicated that bone tissue could be formed both inside and outside of the scaffold materials.

Hematoxylin and eosin (H&E) staining showed that the newly formed bone tissues could be observed in the CMHAP@CL scaffolds (Fig. 4(a)). It could be seen that new bone tissue was formed both on the surface and inside of the scaffold material. Since it was a porous material, bone formation was basically found in the interior of each pore, and angiogenesis could also be seen in the pore, indicating that bone tissue could be formed well in the pore. Similarly, at 12 weeks post-surgery, Masson's trichrome staining (Fig. 4(b)) revealed that only a thin layer of soft tissue and a small fraction of bone/osteoid had formed in both the D-CMHAP@CL and Ach-MHAP@CL scaffolds. Conversely, the L-CMHAP@CL scaffolds elicited a greater quantity of osteoid and mature/mineralized bone formation (indicated by purple staining in Masson's trichrome) within the scaffold materials.

Under a histomorphometric assay, multiple HE staining photos were selected for bone tissue area statistics using ImagePro Plus software, and the results are shown in Fig. 4(c). The total bone formation statistical area of the L-CMHAP@CL scaffolds accounted for 38.6% of the total pore area of the scaffold materials, while that of the D-CMHAP@CL scaffolds and Ach-MHAP@CL scaffolds accounted for 25.8% and 16.9% of the total pore area, respectively. Statistics were also used to assess the number of blood vessels formed in the pores (Fig. 4(d)). In the L-CMHAP@CL scaffolds, 83.0% of the pores were detected with blood vessel formation, while 71.0% and 72.5% of the pores in the D-CMHAP@CL scaffolds and AchMHAP@CL scaffolds were detected, respectively, which was consistent with the findings observed by HE staining. Therefore, it can be concluded that the L-CMHAP@CL scaffolds contribute more to osteogenic growth *in vivo*. The osteogenic ability of the L-/D- and Ach-scaffolds was different, suggesting that chiral scaffolds may possess selectivity for osteogenesis growth *in vivo*. H&E and Masson's trichrome staining after 24 weeks of osteogenesis also showed a similar trend (Fig. S14, ESI†). These results were also consistent with those from SEM and micro-CT, jointly demonstrating that the L-CMHAP@CL scaffolds were more effective in bone formation, namely that chiral scaffolds could selectively induce bone formation.

In order to further demonstrate osteogenic and chiral enantio-selectivity, real-time fluorescence quantitative analysis (RT-qPCR) was used to detect osteogenic genes. The characteristic genes expressed in different osteogenic periods were selected, such as Runx2, Ostrix, and ALP in the early middle stage, and OCN and Col1 in the late stage. As shown in Fig. 5(a), no matter what genes are expressed at the time of osteogenesis, the number of genes expressed in the L-CMHAP@CL scaffolds was always higher than that in the D-CMHAP@CL and Ach-MHAP@CL scaffolds. There were significant differences between L-/D-/AchCMHAP@CL scaffolds, which was consistent with the previous HE staining results, suggesting that L-CMHAP@CL scaffolds were more conducive to osteogenesis growth *in vivo*.

In addition, immunohistochemical staining was performed on early bone transcription factor Runx2 and late osteogenic markers osteopontin (OPN) and osteocalcin (OCN). As shown in Fig. 5(b), Runx2 was the most weakly expressed in the three materials, which probably resulted from Runx2 being an early factor. The samples here were selected after 12 weeks of

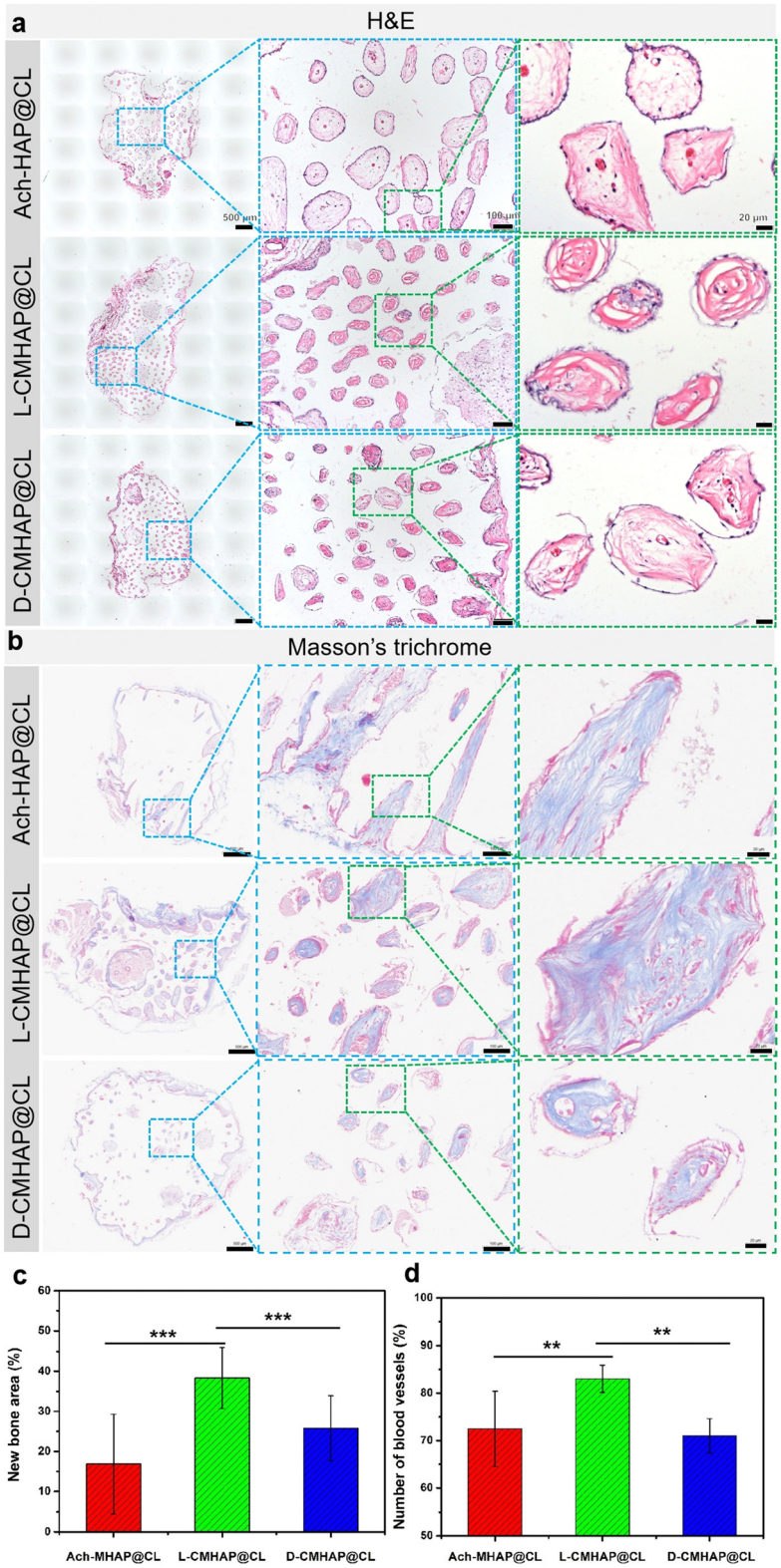

Fig. 4 Histological analysis revealed that chirality selectivity regulates the bone formation capability of the CMHAP@CL scaffolds. (a), (b) H&E and Masson's trichrome staining of the *in vivo* bone formation ability for the Ach-MHAP@CL, L-CMHAP@CL and D-CMHAP@CL scaffolds in nude mice at 12 weeks after operation; the scale bars are 500, 100, and 20 μm. (c) The percentage of new bone area assessed at week 12 after implantation by histomorphometric analysis (n = 6). (d) The percentage of the blood vessel area in the pores in the 2D sectional images was measured (n = 6). Data are presented as mean ± SD. *P < 0.05, **P < 0.01, ***P < 0.001.

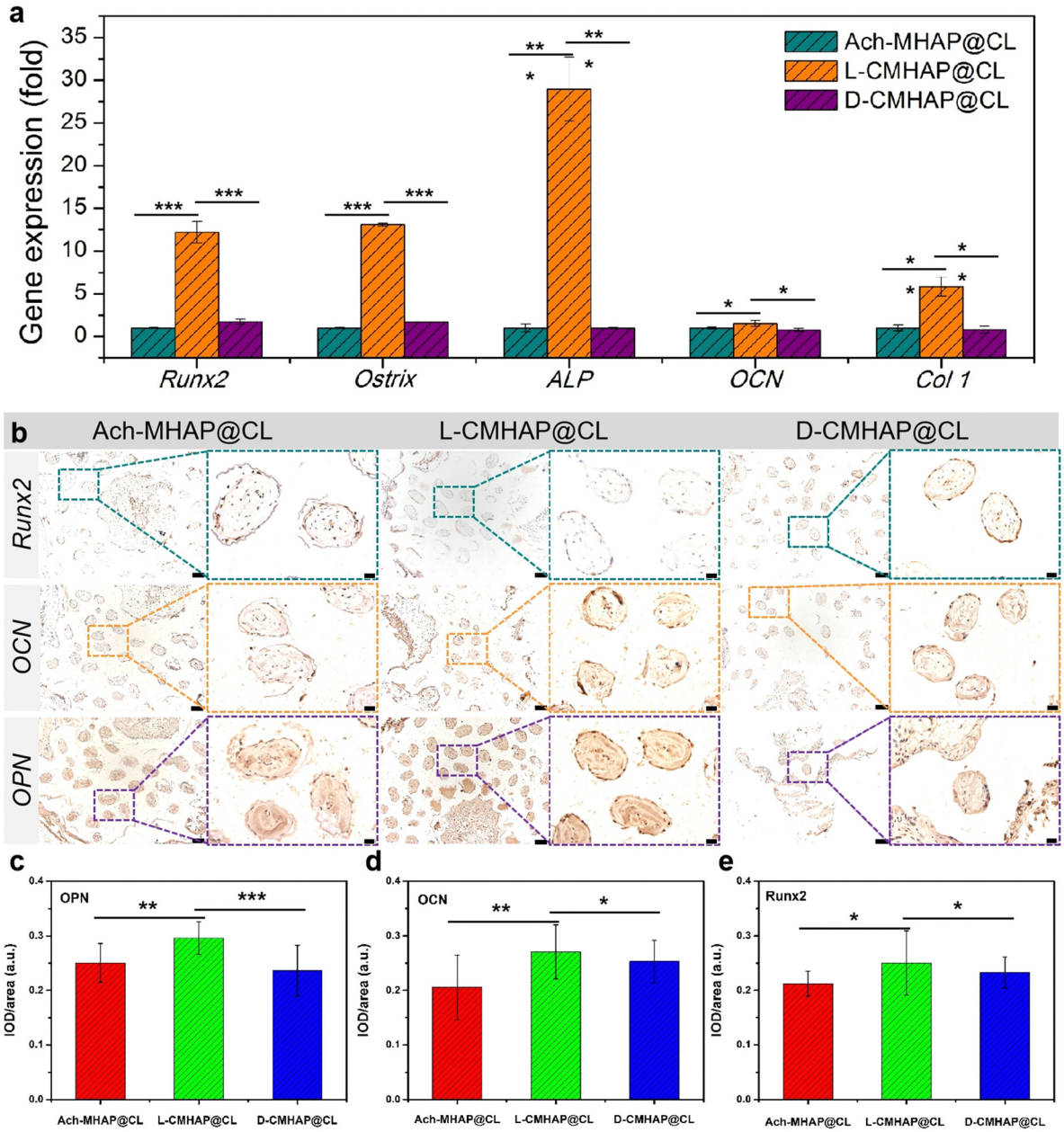

Fig. 5 qPCR and immunohistochemical analysis revealed that chirality selectivity regulates the bone formation capability of the CMHAP@CL scaffolds. (a) RT-qPCR quantification analysis revealing the greatest upregulation of osteogenic markers (Runx2, Ostrix, ALP, OCN and Col1) in the L-CMHAP@CL scaffold. (b) Runx2, OCN and OPN immunostaining of the scaffold after the bone formation at 12 weeks post-surgery; scale bars are 100 and 20 μm. (c), (d), (e) Quantitative analysis of OPN, OCN and Runx2. Data are presented as mean ± SD (*$P < 0.05$, **$P < 0.01$ and ***$P < 0.001$ for groups compared with the control group).

osteogenesis, and were analyzed in the middle and late stages. OPN and OCN were more strongly expressed in the L-CMHAP@CL scaffolds, but there was less expression in the D-CMHAP@CL scaffolds and Ach-MHAP@CL scaffolds, using the naked eye. Quantitative analysis was subsequently conducted using IOD/area values to measure protein expression. As indicated in Fig. 5(c)–(e), OPN, OCN and Runx2 expressions in the L-CMHAP@CL scaffolds were significantly increased, and the IOD/area values were 0.27, 0.29 and 0.25, respectively. The D-CMHAP@CL scaffolds and Ach-MHAP@CL scaffolds had IOD/area values of 0.25, 0.24, 0.23 and 0.20, 0.25, 0.21, respectively. It was demonstrated that there was new bone formation in the scaffolds, and the amount of new bone formation in the L-CMHAP@CL scaffolds was higher than that in the D- and Ach-scaffolds. The immunohistochemical staining after 24 weeks (Fig. S15, ESI†) of osteogenesis also showed a similar trend. These results were all consistent with the results of H&E and Masson's trichrome staining and RT-qPCR, which together demonstrated that L-CMHAP@CL scaffolds contributed significantly to bone formation.

Based on these findings, the biomimetic CMHAP@CL scaffold material could successfully induce the growth of blood vessels and new bone tissue into the biomimetic material, effectively promote bone formation, and show certain selectivity among different chiral structured scaffolds. This chiral selectivity was speculated to be derived mainly from the matching between the space configuration of the osteoblast and the chiral hierarchical structure.[40,41] The chiral micromolecule units in the extracellular matrix (ECM) matched the first-order chiral structures in the CMHAP@CL, and the biomacromolecules in the ECM matched the second-order chiral structures. The osteoblast matched the third-order chiral structures, and the new bone matched with the whole CMHAP@CL scaffolds.

4. Conclusions

In summary, CMHAP@CL scaffolds with chiral mesostructures and surface topographies, including on the atomic scale to the macroscale, were synthesized by self-assembly of a symmetry-breaking chiral molecule and inorganic source. The high asymmetry exhibited by three levels of chirality, ranging from the atomic to micron scale, induces an effective chiral microenvironment that leads to enantioselectivity in the antipodal CMHAP@CL scaffolds. *In vivo* experiments demonstrate that the L-CMHAP@CL scaffolds have significantly improved bone formation ability. To the best of our knowledge, this is the first example of chiral inorganic scaffolds that exhibit excellent bone formation capacity. This work may be promising for the design of bioadaptable bone regeneration materials.

Author contributions

C. F. and S. C. conceived the idea and led the project. C. Z. prepared the CMHAP@CL samples, and performed the XRD, SEM, and DRCD measurements. C. Z., A. L., P. L., and S. Z. completed implantation experiments and related characterization. J. A. and L. H. worked on the structural characterization through HRTEM. C. Z. and B. L. took part in the discussion on CD and cell biology-related work. C. Z., Shuai C., and Y. O. performed the micro-CT measurements. C. Z., S. C. and C. F. contributed to the structural analysis and preparation of the manuscript.

Conflicts of interest

The authors declare no competing financial interests.

Acknowledgements

This work was supported by the National Natural Science Foundation of China (grant no. 21931008, 82272475, 82072452, 8217090787, 82172422), the Key Project of National Natural Science Foundation of China (no. 81830076), Science Foundation of the Shanghai Municipal Science and Technology Commission (19JC1410300), Shanghai Engineering Technology Research Center and Professional Technology Service Platform project of 2020 ''Science and Technology Innovation Action Plan'' of Shanghai (no. 20DZ2254100), National Key R&D Program of China (no. 2021YFC2400801), Biomedical Technology Support Special Project of Shanghai 2021 ''Science and Technology Innovation Action Plan'' (no. 21S31902300), Biomedical Technology Support Special Project of Shanghai 2020 ''Science and Technology Innovation Action Plan'' (no. 20S31900300), Clinical Research Center (CR) of Shanghai University of Medicine and Health Sciences (no. 20MC2020001).

Notes and references

1 L. D. Barron, *Space Sci. Rev.*, 2008, **135**, 187–201.
2 F. Devínsky, *Symmetry*, 2021, **13**(12), 2277.
3 U. G. K. Wegst, H. Bai, E. Saiz, A. P. Tomsia and R. O. Ritchie, *Nat. Mater.*, 2015, **14**, 23–36.
4 P. Fratzl and R. Weinkamer, *Prog. Mater. Sci.*, 2007, **52**, 1263–1334.
5 B. Alexander, T. L. Daulton, G. M. Genin, J. Lipner, J. D. Pasteris, B. Wopenka and S. Thomopoulos, *J. R. Soc., Interface*, 2012, **9**, 1774–1786.
6 N. Reznikov, J. A. M. Steele and P. Fratzl, *Nat. Rev. Mater.*, 2016, **1**(8), 1–14.
7 N. Reznikov, M. Bilton, L. Lari, M. M. Stevens and R. Kröger, *Science*, 2018, **360**, 2189.
8 N. Reznikov, R. Shahar and S. Weiner, *Acta Biomater.*, 2014, **10**(9), 3815–3826.
9 D. J. Buss, R. Kröger and M. D. McKee, *et al.*, *J. Struct. Biol.*, 2022, **6**, 100057.
10 C. Zhou, X. Zhang and J. Ai, *et al.*, *Nano Res.*, 2022, **15**(2), 1295–1302.
11 E. Roddy, M. R. DeBaun and A. Daoud-Gray, *et al.*, *Eur. J. Orthop. Surg. Traumatol.*, 2018, **28**, 351–362.
12 F. Migliorini, G. La Padula, E. Torsiello, F. Spiezia, F. Oliva and N. Maffulli, *Eur. J. Med. Res.*, 2021, **26**(1), 118.
13 W. Wang and K. W. K. Yeung, *Bioact. Mater.*, 2017, **2**(4), 224–247.
14 Q. Ou, P. Wu, Z. Zhou, D. Pan and J. Y. Tan, *BMC Surg.*, 2020, **20**(1), 216.
15 R. Lanza, R. Langer, J. P. Vacanti and A. Atala, *Principles of tissue engineering*, Academic Press, 2020.
16 G. L. Koons, M. Diba and A. G. Mikos, *Nat. Rev. Mater.*, 2020, **5**(8), 584–603.
17 C. F. Guimarães, L. Gasperini and A. P. Marques, *et al.*, *Nat. Rev. Mater.*, 2020, **5**(5), 351–370.
18 A. Ho-Shui-Ling, J. Bolander and L. E. Rustom, *et al.*, *Biomaterials*, 2018, **180**, 143–162.
19 A. I. M. Greer, V. Goriainov and J. Kanczler, *et al.*, *ACS Appl. Mater. Interfaces*, 2020, **12**(30), 33541–33549.
20 L. Zhang, G. Yang and B. N. Johnson, *et al.*, *Acta Biomater.*, 2019, **84**, 16–33.
21 X. Xiao, W. Wang and D. Liu, *et al.*, *Sci. Rep.*, 2015, **5**(1), 9409.

22 L. Bai, Z. Du and J. Du, *et al.*, *Biomaterials*, 2018, **162**, 154–169.
23 B. Fan, Z. Guo and X. Li, *et al.*, *Bioact. Mater.*, 2020, **5**(4), 1087–1101.
24 S. Shirazi, S. Ravindran and L. F. Cooper, *Biomaterials*, 2022, **291**, 121903.
25 Y. Wang, *J. Mater. Sci. Technol.*, 2016, **32**(9), 801–809.
26 X. Xu, Z. Jia and Y. Zheng, *et al.*, *Matter*, 2021, **4**(8), 2648–2650.
27 I. S. Neira, Y. V. Kolen'ko and O. I. Lebedev, *et al.*, *Cryst. Growth Des.*, 2009, **9**, 466–474.
28 Y. Duan, L. Han, J. Zhang and S. Che, *et al.*, *Angew. Chem., Int. Ed.*, 2015, **54**, 15170–15175.
29 Y. Liu, J. Wang, S. Kim, H. Sun, F. Yang, Z. Fang, N. Tamura, R. Zhang, X. Song, J. Wen, B. Z. Xu, M. Wang, S. Lin, Q. Yu, K. B. Tom, Y. Deng, J. Turner, E. Chan, D. Jin, R. O. Ritchie, A. M. Minor, D. C. Chrzan, M. C. Scott and J. Yao, *Nature*, 2019, **570**, 358–362.
30 D. Keller and C. Bustamante, *J. Chem. Phys.*, 1986, **84**, 2972–2980.
31 Y. Duan, X. Liu, L. Han, S. Asahina, D. Xu, Y. Cao, Y. Yao and S. Che, *J. Am. Chem. Soc.*, 2014, **136**, 7193–7196.
32 K. Robbie, D. J. Broer and M. J. Brett, *Nature*, 1999, **399**, 764–766.
33 K. E. Shopsowitz, H. Qi, W. Y. Hamad and M. J. MacLachlan, *Nature*, 2010, **468**, 422–425.
34 T. Bai, J. Ai, L. Liao, J. Luo, C. Song, Y. Duan, L. Han and S. Che, *Angew. Chem., Int. Ed.*, 2021, **60**, 9421–9426.
35 A. Öztürk Kiraz, S. Kaya and C. Gök, *Acta Phys. Pol., A*, 2020, **137**, 1017–1022.
36 P. Rulis, L. Ouyang and W. Y. Ching, *Phys. Rev. B: Condens. Matter Mater. Phys.*, 2004, **70**, 155104.
37 D. W. Green, B. Ben-Nissan and K. S. Yoon, *et al.*, *Trends Biotechnol.*, 2017, **35**(1), 43–54.
38 X. Lin, E. B. Hunziker and T. Liu, *et al.*, *Mater. Sci. Eng., C*, 2019, **96**, 329–336.
39 C. Zhou, S. Zhang and J. Ai, *et al.*, *Chem. Mater.*, 2021, **34**(1), 53–62.
40 F. A. Shah, P. Thomsen and A. Palmquist, *Acta Biomater.*, 2019, **84**, 1–15.
41 N. Kittur, R. Oak and D. Dekate, *et al.*, *Mater. Today: Proc.*, 2021, **43**, 1064–1070.